RSC Advances

PAPER

View Article Online
View Journal | View Issue

Cite this: *RSC Adv.*, 2017, **7**, 55778

Shape-controlled $CoFe_2O_4$ nanoparticles as an excellent material for humidity sensing

Yogendra Kumar,[a] Alfa Sharma [a] and Parasharam M. Shirage *[ab]

Received 8th October 2017
Accepted 27th November 2017

DOI: 10.1039/c7ra11072c

rsc.li/rsc-advances

The humidity sensing performance of cobalt ferrite nanoparticles ($CoFe_2O_4$ NPs) with controlled morphology obtained *via* a solution route is reported in this work. The humidity sensing properties of the presented $CoFe_2O_4$ NPs ferrite sensor were investigated by exposing it to a broad humidity range of 8–97% at room temperature. $CoFe_2O_4$ NPs with spherical, cubic, and hexagonal shapes have been successfully achieved by tuning the growth conditions like reaction time and amount of solvent. These $CoFe_2O_4$ NPs exhibit morphology-dependent chemi-resistive humidity sensing behaviors. The highest humidity sensitivity value of ~590 along with response/recovery value of 25/2.6 s at room temperature was obtained for $CoFe_2O_4$ hexagonal (CF-H) shape as compared to $CoFe_2O_4$ spherical (CF-S) and $CoFe_2O_4$ cubic (CF-C) shapes. Freundlich adsorption isotherm model was well fitted with the experimental results which turned up in support of a plausible humidity sensing mechanism. The morphology-dependent $CoFe_2O_4$ nanostructures exhibit promising sensing capabilities which ensure them as a potential candidate for magnetic recording media and next-generation humidity sensors.

1. Introduction

Humidity is a physio-chemical phenomenon that affects numerous cases leading to deterioration by environmental exposure. Owing to this, and the many areas affected by humidity, there is a need to retain control of humidity. This means that humidity sensors have been of great interest to researchers in recent years. Humidity sensors play a pivotal role in determining the quality of products, precision of instruments, and human life by suitable regulation of humidity for various human comforts.[1,2] Ferrites are currently one of the most investigated nanomaterials due to their characteristics for improvised multifunctional application. In this regard, to obtain effective sensors, the properties can be tuned by changing the material characteristics such as composition, crystallite size, porosity, and shape. Rezlescu *et al.* discussed humidity sensing properties of $MgFe_2O_4$ ferrite with substitution and addition of different cations.[3] Similarly, Seki *et al.* reported ferrites as humidity sensitive by gaining precise insight into the electrical and magnetic characteristics of the materials.[4] A mixed Ni–Co ferrite and the effect of applied calcination temperature on the humidity sensing properties were reported by Virlan *et al.*[5] The humidity sensing of soft ferrites like mixed Cu–Zn system has also been observed where formulation of highly sensitive ferrites by doping was discussed as an alternative to the conventional metal oxide-based humidity sensors.[6] Muthurani *et al.* reported the humidity sensing properties of Cu–, Co– and mixed Cu–Co ferrites where $CuFe_2O_4$ showed better results than others at room temperature.[7] Among the ferrite family, $CoFe_2O_4$ nanoparticles (NPs) have received significant attention due to their inherent magnetic, electrical, and mechanical properties along with high chemical stability.[8,9] Cobalt ferrite NPs are a suitable candidate for various technological applications, such as biosensors,[10] gas sensors,[11–13] stress sensors,[14] magnetic recording media,[8] magneto-optical devices,[9] magnetic resonance imaging,[15] catalysis,[16] biomedical applications,[15] *etc.* No detailed information is available on humidity sensing of cobalt ferrite NPs. Cobalt ferrite has cubic spinel structure, which is mainly interesting for sensing behavior due to its chemical composition and structure, where the presence of more than one cation site modulates the performance due to the variation of chemical nature and oxidation states of cations.[11] Humidity sensors based on metal oxide materials have advantages such as being economical for mass production, and convenient for use in a wide operating range. The ability of a metal oxide to detect the presence of humidity depends on the interaction between water molecules and the surface of the metal oxide, *i.e.*, the reactivity of its surface. The reactivity of the surface depends on the cation distribution and morphology, which mainly depend on the synthesis technique.

Various preparation techniques including hydrothermal method, sol–gel method, co-precipitation method, ball milling, and self-combustion were developed to produce cobalt ferrite nanostructures.[11,17–20] Apart from these techniques, solution-

[a]*Discipline of Metallurgy Engineering and Materials Science, Indian Institute of Technology Indore, Simrol, Indore-453552, India. E-mail: paras.shirage@gmail.com; pmshirage@iiti.ac.in*

[b]*Discipline of Physics, Indian Institute of Technology Indore, Simrol, Indore-453552, India*

based routes are less time consuming and comprehensive to prepare well-dispersed nanostructures with desirable morphology. However, there remain some issues regarding the structure tunability, stability and reproducibility of the prepared nanostructures. Therefore, there is an immediate requirement to find a facile solution route that can directly provide structural tunability of the desired material for diverse applications.

In this study a facile bottom-up solution approach is utilized to obtain nanostructures of $CoFe_2O_4$. Here we highlight three important aspects of the study. First is the direct visualization of different nanostructures of $CoFe_2O_4$, *i.e.* spheres, cubes and hexagons, that attracted our attention to study their morphological properties. Secondly, efforts have been made to study their effects on humidity sensing in detail for the first time. Finally, emphasis has been given to correlate the experimental findings with the available theoretical sensing models, for instance the Freundlich adsorption isotherm model that relates to a plausible sensing mechanism.

2. Experimental details

2.1. Materials

Cobalt(II) acetylacetonate, iron(III) acetylacetonate, oleic acid and benzyl ether were purchased from Sigma-Aldrich and were used as received without any further purification. Here, cobalt(II) acetylacetonate and iron(III) acetylacetonate were used as the precursors. Additionally, oleic acid was utilized as a surfactant and benzyl ether as the solvent.

2.2. Synthesis of $CoFe_2O_4$ nanostructures

Synthesis of $CoFe_2O_4$ spherical (CF-S) NPs. Morphology-controlled CF-S NPs were obtained *via* a solution-based technique. To obtain CF-S NPs, cobalt(II) acetylacetonate (0.6 mM), iron(III) acetylacetonate (1.2 mM), oleic acid (2.5 mL), and benzyl ether (40 mL) were used. The mixture was heated to 100 °C under nitrogen atmosphere for 30 minutes. After that, the reaction temperature was raised to 280 °C for 20 min with refluxing and the color of the solution turned black that indicated the formation of NPs. The solution was cooled down to room temperature, and the precipitate was collected by adding synthetic grade ethanol. The final product was redispersed in hexane for further characterization.

Synthesis of $CoFe_2O_4$ cubic (CF-C) NPs. The same synthesis procedure was followed as for CF-S with a few modifications. Here, for preparing CF-C NPs, 1.2 mM of iron(III) acetylacetonate, 0.6 mM of cobalt(II) acetylacetonate, oleic acid (2.5 mL), and benzyl ether (30 mL) were used. In addition, the refluxing time was increased to 40 minutes.

Synthesis of $CoFe_2O_4$ hexagonal (CF-H) NPs. Similar to the cases of CF-S and CF-C, for the synthesis of CF-H NPs, the amount of benzyl ether was reduced to 20 mL and the refluxing time was increased to 90 minutes, while keeping the other conditions, *i.e.* the amount of precursor and surfactant, unchanged.

2.3. Characterization

Powder X-ray diffraction (XRD) analyses of CF-S, CF-C and CF-H NPs were carried out using an X-ray diffractometer (Bruker D8 Advance) with Cu Kα radiation (λ = 1.540 Å) in the 2θ range from 25° to 70° with a step of 0.30° per minute. The morphologies of as-prepared CF-S, CF-C, and CF-H NPs were determined using high-resolution transmission electron microscopy (HRTEM) with a Tecnai G2 F30 operating at 300 kV. The humidity sensing measurement was done by using a Keithley 2401 source meter and a PC interfaced with LABVIEW.

2.4. Device fabrication and humidity sensing

ITO-coated glass substrates (1 cm × 1 cm) were used for device fabrication. A channel was made on the substrate so that the two sides of the channel will act as source and drain. A channel length of 10 mm and width of 1 mm were maintained. A paste of each of the different $CoFe_2O_4$ NPs individually was then drop-cast into the channel for a series of devices. The devices were dried in a furnace at 50 °C for 30 min and then used for further sensing experiments. The sensing experiment was constructed with saturated aqueous solutions of KOH, $MgCl_2 \cdot 6H_2O$, K_2CO_3, $Mg(NO_3)_2$, $NaNO_3$, NaCl, KCl, and K_2SO_4 in closed conical flasks with a controlled environment with relative humidity (RH) of 8, 33, 43, 52, 63, 75, 86 and 97%, respectively,[21–24] and the RH levels were monitored by a standard hygrometer. The entire experiment was carried out at room temperature.

3. Results and discussion

3.1. Crystal structure analysis

XRD patterns were recorded to determine the phase purity and crystal structure of the as-synthesized CF-S, CF-C, and CF-H NPs, as shown in Fig. 1. The XRD patterns of CF-S, CF-C, and CF-H NPs present diffraction peaks which were indexed to a cubic spinel structure of $CoFe_2O_4$ NPs, in good agreement with previous studies.[25,26] CF-H NPs show intense diffraction peaks as compared to the CF-S and CF-C NPs. The difference in the intensities of the diffraction peaks may suggest a variation of morphology and particle size. Eom *et al.* reported a similar morphology-dependent behavior of diffraction patterns as obtained here.[26] In order to get more insight into the crystallite

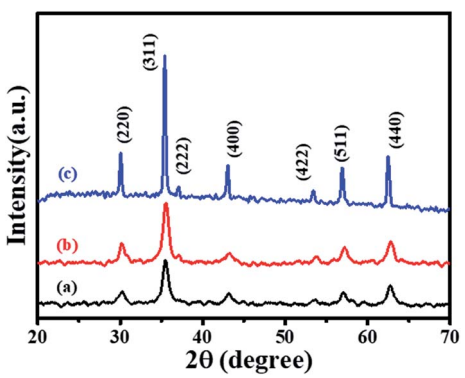

Fig. 1 XRD patterns of (a) CF-S, (b) CF-C, and (c) CF-H NPs.

size and morphology of the as-synthesized CF NPs, the crystallite size was calculated (from XRD patterns) and HRTEM measurements were conducted.

The crystallite sizes of the CF-S, CF-S, and CF-H NPs were calculated from XRD patterns by using the Debye–Scherrer formula[27–30] which can be expressed as:

$$D = \frac{K\lambda}{\beta \cos \theta} \quad (1)$$

where D is the crystallite size, β is the line broadening at full width half maximum (FWHM), θ is the Bragg angle, λ is the wavelength of X-rays, and K is a dimensionless shape factor, which has a value close to unity.

The calculated crystallite sizes of CF-S, CF-C, and CF-H NPs were 22.2, 23.1 and 27.9 nm, respectively. A higher crystallite size of CF-H was observed than that of CF-S and CF-C, which is well expected from the high diffraction peak intensity for CF-H.

Further, the lattice parameters were determined from eqn (2) and (3).[3,29] The formulas can be expressed as:

$$d = a_0\sqrt{h^2 + k^2 + l^2} \quad (2)$$

$$n\lambda = 2d \sin \theta \quad (3)$$

where a_0 is the lattice constant, d is the distance between atomic layers in crystals and (hkl) is the plane indexing. The calculated lattice parameters of CF-S, CF-C, and CF-H NPs were 8.346, 8.348 and 8.356 Å, respectively, which are in agreement with earlier reports.[25]

3.2. Morphology study

The competition between the growth rates of different crystallographic facets determines the final shape of NPs. Surfactants and capping/reducing agents can alter the surface energies of these crystallographic planes and control the growth rates of different crystallographic facets.[31] In addition, several studies have been reported that involved controlling the nucleation and growth dynamics by altering the temperature, heating rate, surfactant and precursor concentration resulting in the formation of different sized and shaped NPs.[26] As mentioned in the Experimental section, in our study, oleic acid was used as a surfactant whereas benzyl ether was used as a solvent. By changing only the reaction time and solvent amount, the shape of the NPs was tuned from spherical (CF-S) to cubic (CF-C) followed by hexagonal (CF-H). Fig. 2(a–c) displays TEM images of CF-S, CF-C and CF-H NPs. The insets of Fig. 2(a–c) present the corresponding particle size distributions of the as-prepared materials. Initially, CF-S NPs (Fig. 2(a)) were formed with an average size of 23.5 nm at 20 min refluxing time. After that, when the refluxing time was increased to 40 min, the shape of CF-S was transformed to CF-C (Fig. 2(b)). Finally, when the refluxing time was increased to 90 min, the shape of CF-C was further transformed to CF-H. In the present study, the transformation of the CF NPs from sphere to hexagon may be attributed to the relationship between the change in solvent amount and reaction time. CF-S NPs were obtained when we used 2.5 mL of oleic acid and 40 mL of benzyl ether for 20 min refluxing at 280 °C, due to isotropic growth in all possible directions. Decreasing the amount of benzyl ether and increasing the reaction time to 40 min increases the growth at a faster rate along the ⟨111⟩ direction with respect to isotropic growth which results in the formation of CF-C NPs. Again, on further reducing the solvent amount to 20 mL and increasing the reaction time to 90 min, the growth along ⟨111⟩ direction gets saturated and the surface along {100} direction enhances to form the hexagonal structure (CF-H NPs). Thus, in CF-H, both {111} and {100} surfaces were developed.[26,32]

HRTEM images of single CF-S, CF-C, and CF-H NPs are shown in Fig. 2(d–f). The spacing between two fringes was measured to be 0.21 nm, 0.29 nm, and 0.47 nm corresponding

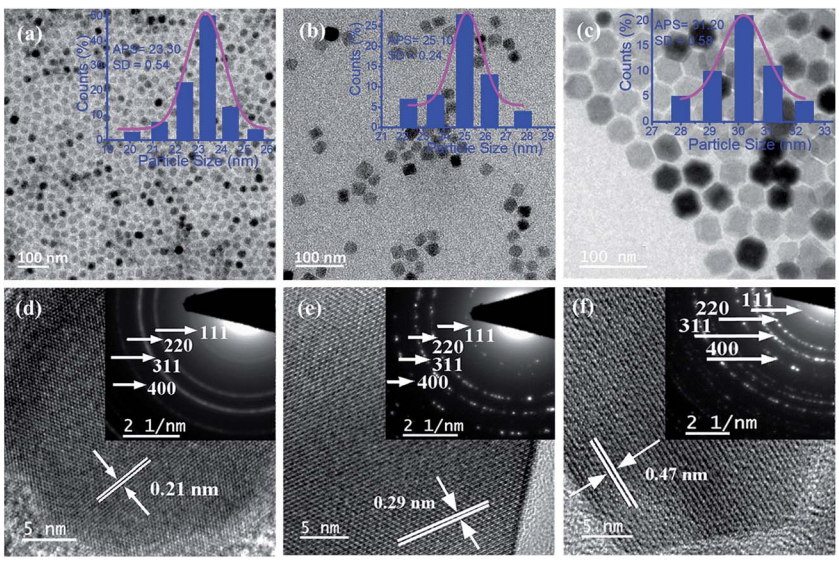

Fig. 2 TEM images of (a) CF-S, (b) CF-C and (c) CF-H NPs (insets show size distribution histograms) and HRTEM images of (d) CF-S, (e) CF-C and (f) CF-H NPs (insets show the SAED patterns).

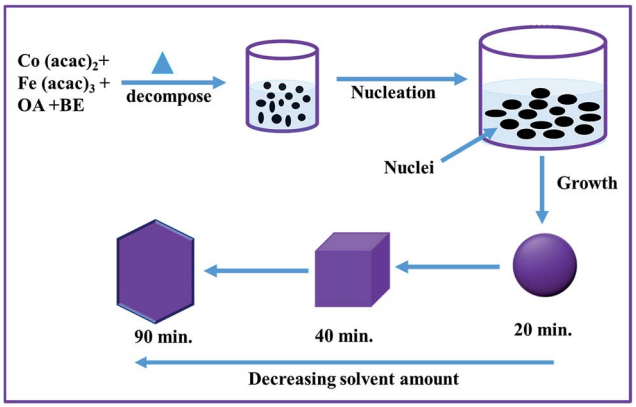

Fig. 3 Schematic illustration of the formation of the various morphologies of $CoFe_2O_4$ NPs through tuning the solvent amount (OA, oleic acid; BE, benzyl ether).

to the interplanar spacing of (400), (220), and (111) planes of $CoFe_2O_4$ NPs (insets show the selected area electron diffraction (SAED) patterns). From the SAED and HRTEM analysis, we found that all of the CF-S, CF-C and CF-H NPs possess spinel crystalline structure which is in agreement with the obtained XRD results.[32]

From the above discussed results, we found that the amount of surfactant/solvent and reaction time play crucial role for the transformation of CF-S to CF-C, and then to CF-H NPs. A schematic illustration of the proposed formation of different shapes of $CoFe_2O_4$ NPs is provided in Fig. 3.

Furthermore, to investigate the effect of reaction time on the morphology of $CoFe_2O_4$ NPs, the refluxing time of the reaction was maintained for 30, 60 and 90 min. Fig. 4 shows TEM images of NPs obtained at different refluxing time while keeping other reaction conditions constant, *i.e.*, precursor concentration, ratio of reducing agent and solvent amount. Monodisperse nearly sphere-like shapes of $CoFe_2O_4$ NPs with average size of 24.22 nm, 29.94 nm, 33.68 nm were observed for the 30, 60 and 90 min reaction refluxing times, respectively. Larger particle size was observed for the longer refluxing time whereas the shape of the NPs remains almost the same. These results suggest that very similar shape (sphere) of NPs with different size may be achieved by varying the refluxing time, by keeping other reaction conditions as such. Gao *et al.*[32] and Lu *et al.*[33] reported that the size of the NPs increased with prolonging reaction time while the shape of the NPs remains very similar, *i.e.*, sphere, cube, and star, for different precursors and reducing/surfactant concentrations.

3.3. Humidity sensing

In the present study, we investigated the influence of different morphologies of $CoFe_2O_4$ NPs on humidity sensing. In this context, comparisons for all three sensors with spherical (CF-S), cubic (CF-C), and hexagonal (CF-H) cobalt ferrite NPs are shown in Fig. 5(a & b). The measurements were conducted by exposing all the sensors to 8% to 97% RH environment.

The sensitivity of the sensors shows a significant increase with increase in humidity. The sensitivity of humidity sensors was calculated using the equation

$$S\ (\%) = \frac{R_{08\%} - R_x}{R_x} \quad (4)$$

where S (%) is sensitivity, and $R_{08\%}$ and R_x are the resistance of the device at lowest humidity and after the change in humidity, respectively.[34,35] From Fig. 5(b), it is observed that CF-S shows a sudden increase in sensitivity up to ~417% at 97% RH. Similarly, a periodic decrease in resistance and increase in sensitivity up to ~274% was observed for CF-C NPs with an increase in RH. Whereas, CF-H NPs showed a higher sensitivity of ~590%, nearly 2.15 and 1.41 times higher than that of the CF-C and CF-S NPs.

A hysteresis study has practical utility for any electronic device application where minimizing the hysteresis error is crucial. To calculate the hysteresis of the CF-H, CF-S, and CF-C NPs sensor devices, the resistances of the devices were measured at various RH levels. Hysteresis is defined as the drift in resistance of the sensors on increasing RH from 8% to 97% and back from 97% to 8%. The hysteresis of the humidity sensors based on different morphologies is shown in Fig. 6. The hysteresis indicates the different rates of adsorption and desorption of water vapor during the sensing process.

The hysteresis error (H_e) values were determined from eqn (5) at different levels of RH for CF-S, CF-C, and CF-H NPs and can be given as:

$$H_e = \pm \frac{\Delta R_{max}}{2F_{FS}} \quad (5)$$

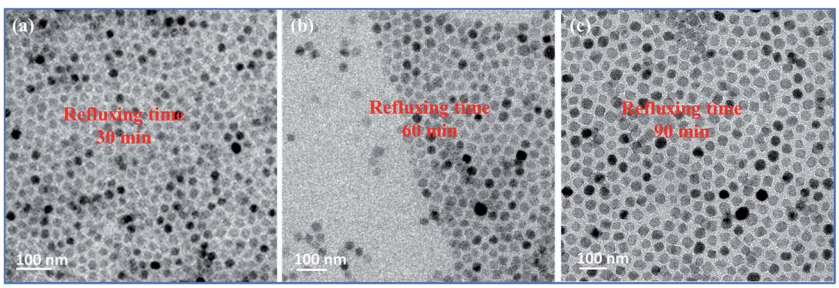

Fig. 4 TEM images of the as-synthesized $CoFe_2O_4$ NPs with nearly sphere-like shapes and different sizes of (a) 24.22 nm, (b) 29.94 nm, and (c) 33.68 nm for different refluxing times.

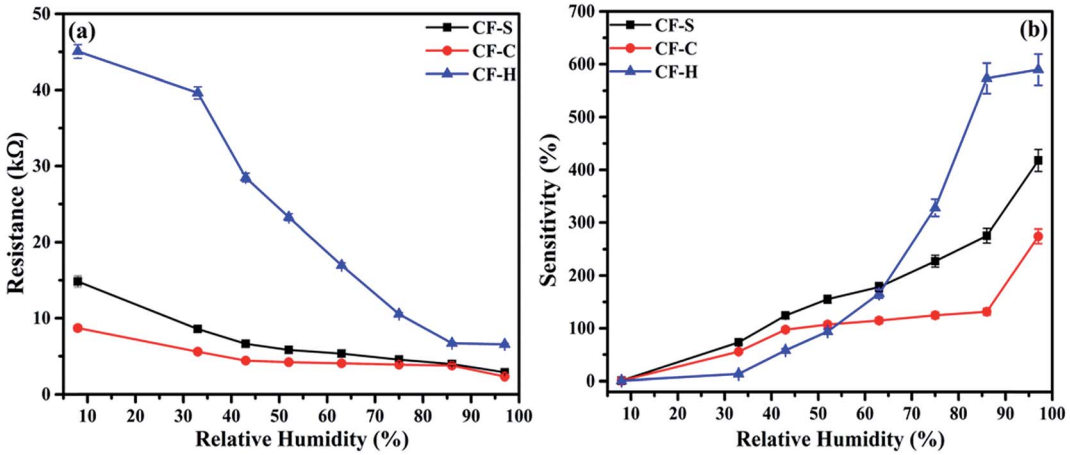

Fig. 5 Plots of (a) resistance and (b) sensitivity *vs.* relative humidity for $CoFe_2O_4$-based RH sensors.

where H_e is the hysteresis error, ΔR_{max} is the difference in the output for the process of adsorption and desorption, and F_{FS} is the full-scale output.[36,37] During the whole adsorption–desorption process, the maximum absolute value of H_e was found to be negligibly small, for each of CF-S, CF-C, and CF-H, providing a better reliability of the sensors.

Response/recovery transient study of any sensing material provides a measure of the operational ability of a device. The response time (T_{res}) was the time taken to achieve 90% change in the total resistance by switching the sensors ON from 8% to 97% RH and recovery time was calculated when sensors moved from 97% to 8% RH. Fig. 7(a–c) presents the response/recovery time of CF-S, CF-C and CF-H which has values of 50.4/3.54 s, 49/3.0 s and 25/2.6 s respectively generally for one cycle of adsorption and desorption. The repeatability behavior of all the cobalt ferrite-based RH sensors was investigated for nearly 9–10 iterative cycles. It can be clearly observed that on transformation of spherical to hexagonal $CoFe_2O_4$ NPs, the response and recovery time of the sensor has been decreased to a great extent.

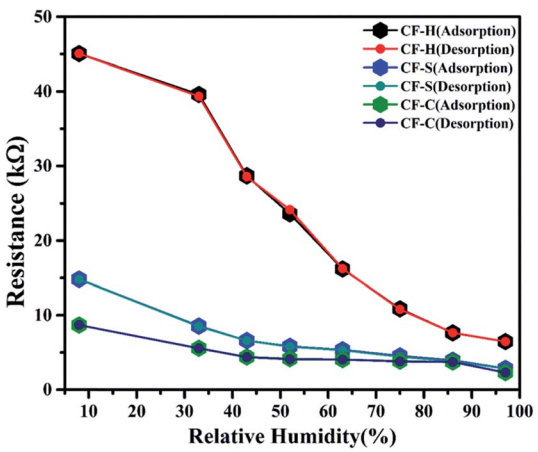

Fig. 6 Hysteresis characteristics of the prepared $CoFe_2O_4$ (CF-H, CF-S, and CF-C) RH sensors.

Long-term stability is one of the important factors for estimating the operational reliability of a sensor device. The stability of resistance of CF-S, CF-C, and CF-H NPs based sensors was measured in different RH and monitored continuously for 7–8 weeks as shown in Fig. 8(a–c).

3.4. Freundlich adsorption isotherm model

When a sensor is subjected to a humidity atmosphere different from ambient, a new adsorption–desorption equilibrium is observed *via* van der Waals forces and hydrogen bonding between adsorbed water molecules and surface-active groups.[38] Considering that ferrites have a number of water adsorption sites in the form of multi-cation sites, the Freundlich adsorption isotherm model appeared to be more appropriate for explaining the surface behavior in the humidity sensing process. The relationship between S (relative deviation in resistance as a function of solute adsorbed on the adsorbent) and C (percent relative humidity as a function of water vapor concentration) can be expressed as $S = k \times C^{\alpha}$, where k and α are the proportionality and exponent constants and represent the adsorption capacity and adsorption strength.[38–40]

The Freundlich adsorption model was applied to investigate the water adsorption–desorption behavior of CF-S, CF-C, and CF-H NPs based humidity sensors. Relative deviation in resistance (ΔR_H) is also an important factor describing the resistance variation of a humidity sensor, which is expressed as

$$\Delta R_H\,(\%) = (R_{LH} - R_H)/R_{LH} \times 100 \quad (6)$$

where R_{LH} is the resistance of samples at low RH (8%) and R_H is the resistance of samples at higher RH. Fig. 9(a) shows relative deviation in resistance (ΔR_H) as a function of applied relative humidity, while Fig. 9(b) displays log–log plots of ΔR_H *vs.* percent relative humidity for CF-S, CF-C, and CF-H. From Fig. 9(a) it is observed that all samples show two significant regions, related to the conduction mechanism, where regions before and after transition point (T_c) were ascribed to charge conduction through chemisorbed and physisorbed layers respectively. Fig. 9(b) shows the experimental data of all three

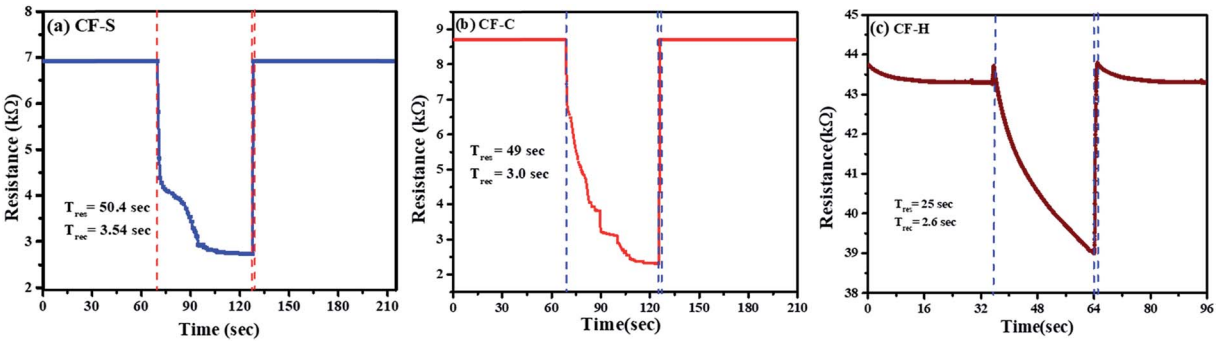

Fig. 7 Response/recovery characteristics of different $CoFe_2O_4$ morphology-based humidity sensors: (a) CF-S, (b) CF-C and (c) CF-H NPs based humidity sensors in 33% to 97% RH.

samples linearly fitted to the Freundlich adsorption model. Two linear regions are attributed to different adsorption regimes, one for lower RH (8–52%) and another at higher RH (≥52%). The T_c value was determined by calculating the point where the two separately modeled linear fits cross each other. The T_c values for CF-S, CF-C, and CF-H were observed at 42.22%, 39.46%, and 61.24% respectively. The Freundlich model constants k and α were determined separately for both regions and are listed in Table 1. It is reported that the higher the α value, the stronger is the adsorption. Table 1 shows that the α value for all $CoFe_2O_4$ NPs based humidity sensors lies above unity within the low RH range, indicating a strong affinity for water vapor. Whereas an opposite trend was observed for all samples in the high RH region where the CF-H sensor showed the highest α value of 0.75 compared to that of CF-S (0.52) and CF-C (0.65) indicating weak adsorption. The overall trend of α values for cobalt ferrite NPs hints towards an increase in the number of surface active sites or exposed facets due to the variation in morphology. A change in the number of exposed facets like {111} and {100} with tuning the particle morphology causes increased humidity sensitivity in the case of CF-H. In this regard the observed trend in adsorption capacity for all the

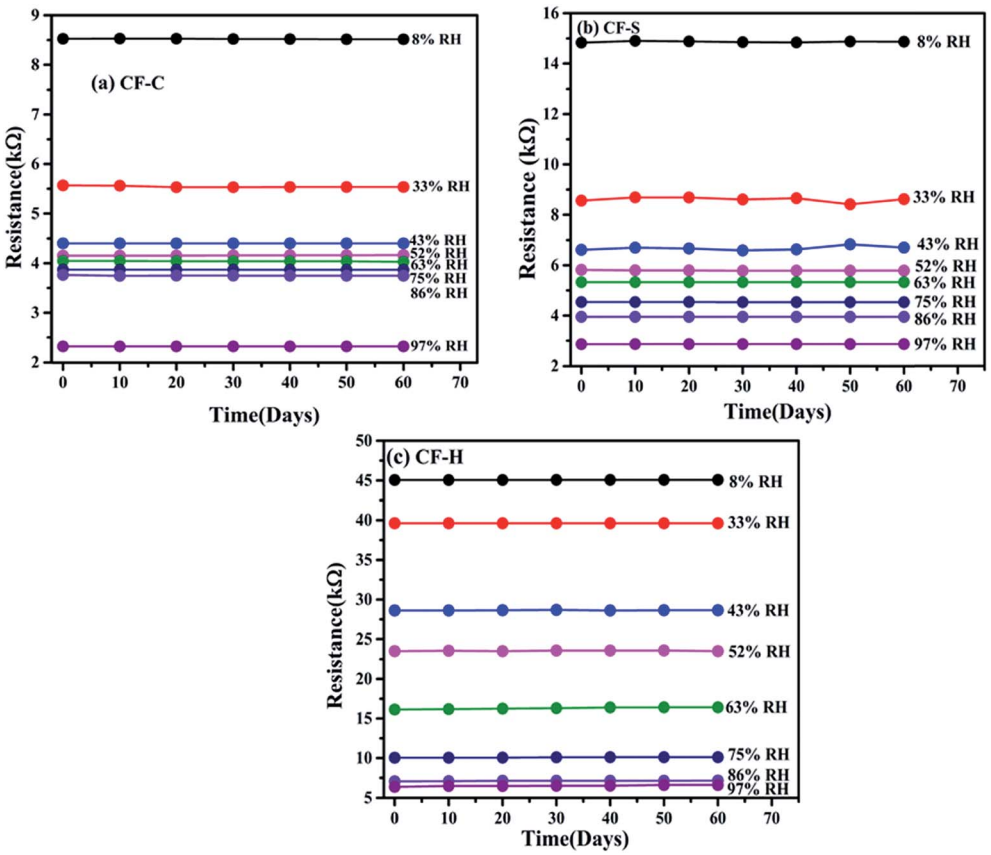

Fig. 8 Long-term stability of (a) CF-C, (b) CF-S and (c) CF-H sensors from 8% to 97% RH at room temperature.

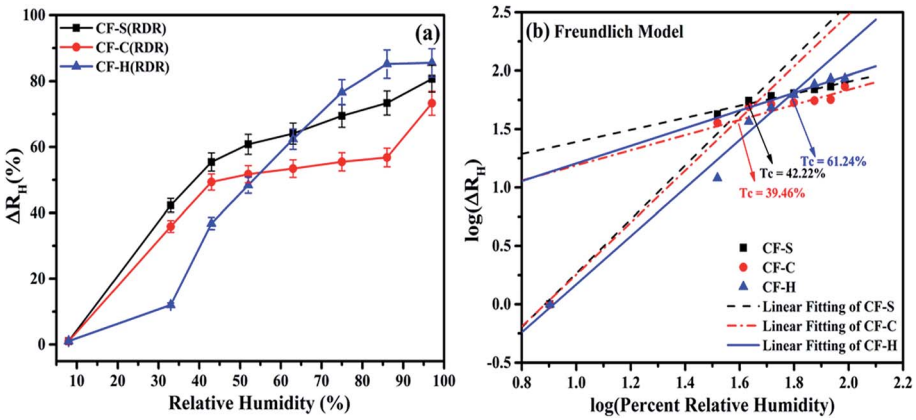

Fig. 9 (a) Relative deviation in resistance (ΔR_H) as a function of applied relative humidity. (b) log–log plot of ΔR_H *vs.* percent relative humidity for CF-S, CF-C, and CF-H.

Table 1 Freundlich adsorption model results including the adsorption capacity (k), adsorption strength (α), and the fitting parameter (R^2) for humidity sensing of CF-S, CF-C, and CF-H

Sample	RH range (%)	k	α	R^2
CF-S	08–52	1.11 ± 0.35	2.31 ± 0.24	0.96
CF-S	52–97	7.48 ± 0.10	0.52 ± 0.05	0.96
CF-C	08–52	3.47 ± 0.57	2.23 ± 0.22	0.96
CF-C	52–97	9.40 ± 0.33	0.65 ± 0.30	0.94
CF-H	08–52	2.82 ± 0.33	2.06 ± 0.208	0.96
CF-H	52–97	7.76 ± 0.30	0.75 ± 0.18	0.95

sensor samples was accounted for from the stronger intermolecular interaction between adsorbate and adsorbent based on the presence of exposed facets.

A better correlation between the experimental and fitted results from the Freundlich model observed in Fig. 9(b) provides a better insight into a plausible sensing mechanism of metal oxide semiconductor-based humidity sensors. The widely accepted humidity sensing mechanism suggests the role of electrons as a key player to control the sensing behavior for a low-humidity environment as protons (H^+) cannot move freely in immobile chemisorbed and initially physisorbed water layers over the sensor surface. On exposure to a high-humidity environment, the H^+ started freely moving in the high level of physisorbed water layers dominating the protonic conduction over the electronic conduction through the Grotthuss chain reaction over the surface. Besides this, the previously adsorbed and ionized oxygen species (O^- and O^{2-}) on the sensor surface affect the mechanism of water molecule adsorption and desorption. The above discussed Freundlich adsorption isotherm model describes this more clearly where experimental evidence points to RH-dependent conduction process taking place.

4. Conclusion

$CoFe_2O_4$ NPs with different morphologies were synthesized by using a facile and economical solution route. XRD shows that the NPs have pure spinel phase structure. TEM images indicate that particle sizes of CF-S, CF-C, and CF-H are 23.5 nm, 25 nm, and 30 nm, respectively. The morphologies of the NPs were very well controlled by varying the surfactant to solvent ratio and reaction time. The humidity sensing properties of the $CoFe_2O_4$ NPs was examined by exposing them to a broad humidity range of 8–97% at room temperature. Humidity sensitivity improved considerably along with response/recovery value of 25 s/2.6 s for CF-H. This is the first detailed report on humidity sensing by $CoFe_2O_4$. Possible fitting with the Freundlich model was attempted and provides better insight into the adsorption–desorption mechanism over the surface of CF-S, CF-C, and CF-H NPs based sensors. The morphology-dependent humidity sensing performance of cobalt ferrite NPs indicates that they are most suitable for room temperature-based next-generation high-performance humidity sensors.

Conflicts of interest

There are no conflicts to declare.

Acknowledgements

This work was supported by the Department of Science and Technology, India by the award of the prestigious 'Ramanujan Fellowship' (SR/S2/RJN-121/2012) to PMS. The authors also acknowledge CSIR research grant no. 03(1349)/16/EMR-II and support from SIC, IIT Indore for providing the XRD and FT-IR characterization facility. The authors are grateful to Professor Pradeep Mathur, director IIT Indore. Y. K. and A. S. acknowledge MHRD fellowship for doctoral research.

References

1 X. Song, Q. Qi, T. Zhang and C. Wang, *Sens. Actuators, B*, 2009, **138**, 368–373.
2 K. Sager, G. Gerlach and A. Schroth, *Sens. Actuators, B*, 1994, **18**, 85–88.

3 N. Rezlescu, E. Rezlescu, P. D. Popa and F. Tudorache, *J. Optoelectron. Adv. Mater.*, 2005, **7**, 907–910.
4 K. Seki, J. I. Shida and K. Murakami, *IEEE Trans. Instrum. Meas.*, 1998, **37**, 468–470.
5 C. Virlan, F. Tudorache and A. Pui, *Int. J. Appl. Ceram. Technol.*, 2017, 1–9, DOI: 10.1111/ijac.12706.
6 A. Vaingankar, S. Kulkarni and M. Sagare, *J. Phys. IV*, 1997, **7**, 155–156.
7 S. Muthurani, M. Balaji, S. Gautam, K. H. Chae, J. H. Song, D. P. Padiyan and K. Asokan, *J. Nanosci. Nanotechnol.*, 2011, **11**, 5850–5855.
8 S. E. Shirsath, X. Liu, Y. Yasukawa, S. Li and A. Morisako, *Sci. Rep.*, 2016, **6**, 30074.
9 F. Choueikani, F. Royer, D. Jamon, A. Siblini, J. J. Rousseau and S. Neveu, *Appl. Phys. Lett.*, 2009, **94**, 051113.
10 D. M. Bruls, *et al.*, *Lab Chip*, 2009, **9**, 3504–3510.
11 (*a*) X. F. Chu, D. Jiang, Y. Guo and C. Zheng, *Sens. Actuators, B*, 2006, **120**, 177; (*b*) A. Sutka and K. A. Gross, *Sens. Actuators, B*, 2016, **222**, 95–105.
12 M. S. Khandekar, N. L. Tarwal, I. S. Mulla and S. S. Suryavanshi, *Ceram. Int.*, 2014, **40**, 447–452.
13 S. Tao, F. Gao, X. Q. Liu and O. T. Sorensen, *Mater. Sci. Eng., B*, 2000, **77**, 172–176.
14 J. A. Paulsen, A. P. Ring, C. C. H. Lo, J. E. Snyder and D. C. Jiles, *J. Appl. Phys.*, 2005, **97**, 044502.
15 O. Veiseh, J. W. Gunn and M. Zhang, *Adv. Drug Delivery Rev.*, 2010, **62**, 284–304.
16 S. Shylesh, V. Schünemann and W. R. Thiel, *Angew. Chem., Int. Ed.*, 2010, **49**, 3428–3459.
17 J. G. Lee, J. Y. Park and C. S. Kim, *J. Mater. Sci.*, 1998, **33**, 3965–3968.
18 X. Li, G. Chen, Y. P. Lock and C. Kutal, *J. Mater. Sci. Lett.*, 2002, **21**, 1881.
19 P. N. Vasambekar, C. B. Kolekar and A. S. Vaingankar, *J. Mater. Sci.: Mater. Electron.*, 1999, **10**, 667.
20 C. Cannas, A. Falqui, A. Musinu, D. Peddis and G. Piccaluga, *J. Nanopart. Res.*, 2006, **8**, 255–267.
21 A. M. Dumitrescu, G. Lisa, A. R. Iordan, F. Tudorache, I. Petrila, A. I. Borhan, M. N. Palamaru, C. Mihailescu, L. Leontie and C. Munteanu, *Mater. Chem. Phys.*, 2015, **156**, 170–179.
22 V. Jeseentharani, M. George, B. Jeyaraj, A. Dayalan and K. S. Nagaraja, *J. Exp. Nanosci.*, 2013, **8**, 358–370.
23 L. Greenspan, *J. Res. Natl. Bur. Stand., Sect. A*, 1977, **81**, 89–96.
24 D. R. Lide, *CRC Handbook of Chemistry and Physics*, CRC Press, Boca Raton, FL, 90th edn, 2010.
25 Y. Kumar and P. M. Shirage, *J. Mater. Sci.*, 2017, **52**, 4840–4851.
26 Y. Eom, M. Abbas, H. Y. Noh and C. G. Kim, *RSC Adv.*, 2016, **6**, 15861–15867.
27 A. K. Rana, Y. Kumar, N. Saxena, R. Das, S. Sen and P. M. Shirage, *AIP Adv.*, 2015, **5**, 097118.
28 Y. Kumar, A. K. Rana, P. Bhojane, M. Pusty, V. Bagwe, S. Sen and P. M. Shirage, *Mater. Res. Express*, 2015, **2**, 105017.
29 R. Das, A. Kumar, Y. Kumar, S. Sen and P. M. Shirage, *RSC Adv.*, 2015, **5**, 60365.
30 A. K. Rana, R. Das, Y. Kumar, S. Sen and P. M. Shirage, *Appl. Surf. Sci.*, 2016, **379**, 23–32.
31 H. Khurshid, L. Wanfeng, S. Chandra, M. H. Phan, G. C. Hadjipanayis, P. Mukherjee and H. Srikanth, *Nanoscale*, 2013, **5**, 7942–7952.
32 G. Gao, X. Liu, R. Shi, K. Zhou, Y. Shi, R. Ma, E. T. Muromachi and G. Qiu, *Cryst. Growth Des.*, 2010, **10**, 2888–2894.
33 L. T. Lu, N. T. Dung, L. D. Tung, C. T. Thanh, O. K. Quy, N. V. Chuc, S. Maenosono and T. K. Thanh, *Nanoscale*, 2015, **7**, 19596–19610.
34 A. S. Pawbake, R. Waykar, D. J. Late and S. R. Jadkar, *ACS Appl. Mater. Interfaces*, 2016, **5**, 3359–3365.
35 P. K. Kannan, D. J. Late, H. Morgan and C. S. Rout, *Nanoscale*, 2015, **7**, 13293–13312.
36 J. Herran, I. Fernandez, E. Ochoteco, G. Cabanero and H. Grande, *Sens. Actuators, B*, 2014, **198**, 239–242.
37 V. K. Tomer, N. Thangaraj, S. Gahlot and K. Kailasam, *Nanoscale*, 2016, **8**, 19794–19803.
38 C. D. Hatch, J. S. Wiese, C. C. Crane, K. J. Harris, H. G. Kloss and J. Baltrusaitis, *Langmuir*, 2012, **28**, 1790–1803.
39 A. Sharma, P. Bhojane, A. K. Rana, Y. Kumar and P. M. Shirage, *Scr. Mater.*, 2017, **128**, 65–68.
40 C. H. Xu, S. Q. Shi and C. Surya, *Sensors*, 2008, **9**, 9903–9924.